Wind Tunnel Testing of a Blown Flap Wing

Devansh R. Agrawal, Faisal As'ad, Blake Berk, Trevor Long, Jackson Lubin*, Christopher Courtin, Jacqueline Thomas†, R. John Hansman‡, Mark Drela§

Massachusetts Institute of Technology, Cambridge, 02139, USA

This paper presents wind tunnel measurements of blown flapped airfoil performance for application to distributed electric propulsion STOL aircraft. The 2D airfoil wind tunnel model features a simple slotted flap, and closely-spaced spanwise-distributed propellers driven by electric motors. Measurements of lift, pitching moment and net streamwise force (drag minus thrust) were made over a range of propeller RPM, angle of attack and flap angle. Lift coefficients up to 9 were measured for practical blowing levels. High lift was also measured with net streamwise force close to zero, which suggests that the use of blown lift during landing is practical.

I. Nomenclature

b	model span
c	chord
Δc_E	jet excess power coefficient
Δc_{EB}	jet excess power coefficient of blowing
Δc_{EH}	jet excess power coefficient of hovering
Δc_J	jet momentum-excess coefficient
c_l	lift coefficient
c_m	pitching moment coefficient
c_x	net streamwise force coefficient (drag–thrust)
h	jet height
h_d	effective 2D actuator disk height
L'	lift force per unit span
M'	moment per unit span
R	propeller radius
Re	chord Reynolds number
r_h	propeller hub radius
u_j	center-line jet velocity
V_∞	freestream velocity
V_J	jet velocity
w	vortex-sheet velocity
x_p, z_p	x, z position of the propeller
α	angle of attack
δ_m	motor axis angle below horizontal
δ_f	flap deflection angle
θ	angle of streamline from the x-axis
γ	vortex strength
κ	streamline curvature
ρ	density

*Undergraduate Student, Aeronautics and Astronautics, MIT, 77 Mass Ave, Cambridge MA, 02139, AIAA Student Member.

†Graduate Student, Aeronautics and Astronautics, MIT, 77 Mass Ave, Cambridge MA, 02139, AIAA Student Member.

‡T. Wilson Professor, Aeronautics and Astronautics, MIT, 77 Mass Ave, Cambridge MA, 02139, AIAA Fellow.

§Terry J. Kohler Professor, Aeronautics and Astronautics, MIT, 77 Mass Ave, Cambridge MA, 02139, AIAA Fellow.

II. Introduction

Recently, interest in aerial urban transportation concepts (commonly known as Urban Air Mobility or UAM) and the maturation of electric aircraft propulsion technology has led to many projects developing vehicles that can operate from takeoff and landing areas (TOLAs) small enough to fit in dense urban settings. While almost all current projects are for vertical takeoff and landing (VTOL) vehicles, several recent studies have suggested that short takeoff and landing (STOL) aircraft may be able to operate off of similarly sized TOLAs through the use of externally blown flaps across most of the aircraft wing [1, 2]. In this blown wing concept, the wake from electric motors distributed along the wing leading edge interacts with the trailing edge flaps to provide much larger effective lift coefficients than are possible with conventional high-lift systems.

Compared to VTOL vehicle concepts, STOL aircraft may have improved mission performance (in terms of range, payload, or speed for a given vehicle size) and an easier pathway to certification [3]. To accurately assess the utility of blown lift vehicles and the feasibility of extreme short-field performance, the effectiveness of the blown flaps and the required power to generate high c_l must be accurately understood. Several aircraft, such as the Boeing C-17 or Lockheed F-104, have used some variation of blown surfaces to support high wing loading. However, due to the relative novelty of the distributed electric configuration, the performance of a fully blown wing STOL aircraft is difficult to predict with high confidence from the existing literature or available computational methods.

In this paper, a wind tunnel study of a blown wing section is presented, with the aim of experimentally characterizing and understanding the aerodynamic performance of a blown lift system. A theoretical framework for understanding and assessing wing blowing is presented in Section III. Section IV describes the experimental design, and results are presented and discussed in Section V.

III. Blown Airfoil Theory

A blown airfoil has a jet of high-velocity air (relative to the freestream) directed over its surfaces. In this paper, we will consider the case of blowing achieved by a propeller modeled as an actuator disc, blowing air mostly under the airfoil.

A. Physical Mechanism

The main underlying mechanism which contributes to increased lift of blown airfoils is the delayed bursting of the main-element wake and the delayed separation of the flap boundary layer [4]. This effect is mainly achieved through the injection of the blowing jet's high total pressure through the flap gap. The end result of this effect is an the airfoil can achieve higher lift through operation at both higher angles of attack, α, and higher flap deflections, δ_f.

An additional mechanism that contributes to increased lift is the downward deflection of the blowing jet, which leaves the wing trailing edge at some downward angle θ_{TE}. The jet's vertical momentum change is associated with an increased pressure on the airfoil bottom surface, which results in an added upward lift force on the wing.
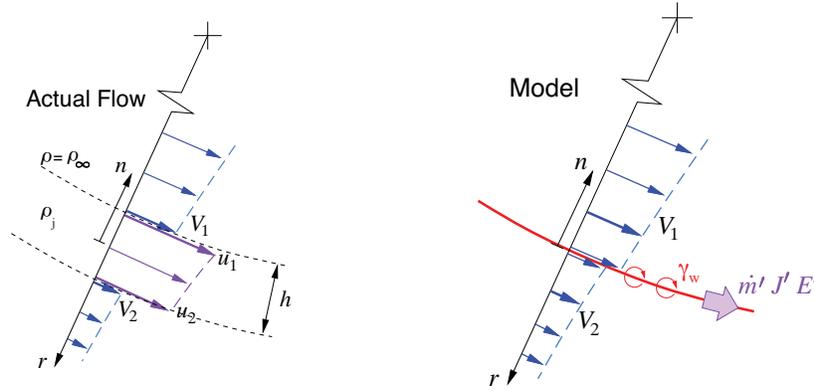
B. Vortex Sheet Model

In thin airfoil theory, following the formulation of Thwaites [5] and Maskell and Spence [6], an airfoil can be modeled by a vortex sheet placed along the the x-axis, as in fig 1. The effect of blowing is captured by adding a jet wake vortex sheet of strength $\gamma_w(x)$, shown in Figure 2, which turns from the trailing edge direction, $\theta(x=c) = \theta_{TE}$ to the final direction $\theta \to \alpha$. To model the forces on the airfoil, we first determine the strength of the wake vortex, and then determine the circulation around the main airfoil, and combine these to determine lift and moments acting on the airfoil.
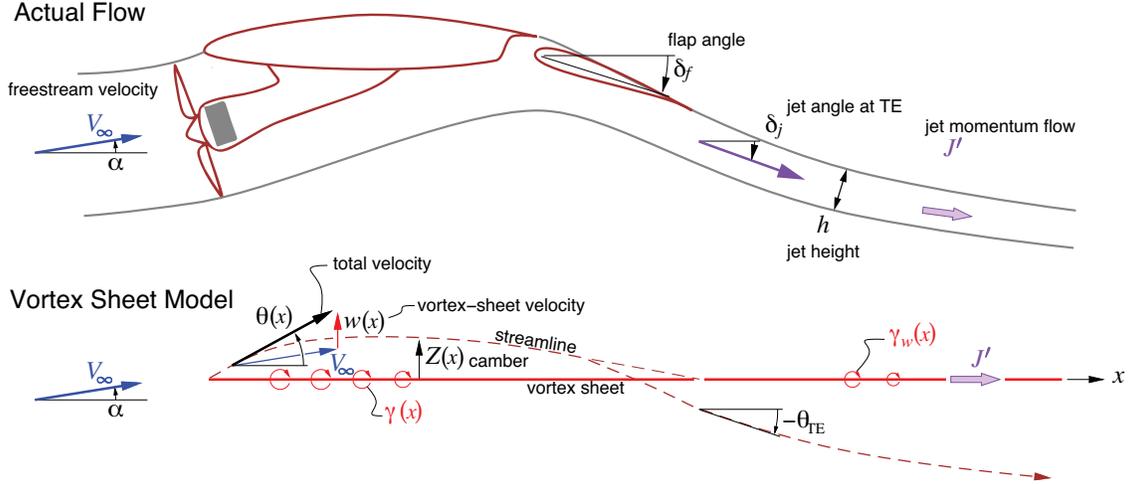
Fig. 1 Actual blown airfoil flow, and vortex sheet model.

1. Jet model

Fig. 2 Jet sheet of finite thickness h, and vortex sheet model. The turning of the jet's momentum-excess $\Delta J'$ implies an apparent pressure load on the vortex sheet.

The jet wake vortex strength is determined by the curvature of the jet stream, $\kappa = \frac{d\theta}{ds}$ as in Figure 2. The potential flow inside the jet will have a free-vortex distribution, $u \sim 1/r$, and, therefore, the jet speed near the center-line is approximately $u(n) = u_a(1 + \kappa n)$ where $u_a \equiv u(0)$ is defined as the average velocity, and n is the normal direction.

Since the pressure is continuous across the jet boundaries, the velocity jumps are related by Bernoulli. The calculated pressure jump across the jet must be equivalent, whether computed using the outer flow velocities or the jet flow velocities. Therefore, the velocity jumps $\Delta V = V_1 - V_2$, $\Delta u = u_1 = u_2$ in Figure 2 are

$$\frac{1}{2}\rho\left(V_1^2 - V_2^2\right) = \frac{1}{2}\rho_j\left(u_1^2 - u_2^2\right) \tag{1}$$

$$\rho V_a \Delta V = \rho_j u_a \Delta u = \rho_j u_a^2 \kappa h \tag{2}$$

where $V_a = (V_1 + V_2)/2$ is the average velocity. The vortex strength is related to the velocity jump, extrapolated to the center-line

$$\gamma_{\mathrm{w}} = V_1\left(1 - \frac{1}{2}\kappa h\right) - V_2\left(1 + \frac{1}{2}\kappa h\right) = \Delta V - V_a \kappa h = \frac{\rho_j u_a^2 - \rho V_a^2}{\rho V_a}\kappa h \tag{3}$$

3

Approximating $V_a \simeq V_\infty$ and $u_a \simeq u_j$, the jet velocity, we define the jet momentum per unit span as

$$J' = \frac{1}{2}\rho_\infty V_\infty^2 c c_J \equiv \int_{-h/2}^{h/2} \rho u^2 \, dn \simeq \rho_j u_j^2 h \tag{4}$$

Therefore the vortex strength is related to the jet momentum-excess J',

$$\frac{\gamma_w}{V_\infty} = \frac{\Delta J'}{\rho_\infty V_\infty^2}\kappa \simeq \frac{\Delta c_J}{2} c \frac{d\theta}{dx} \tag{5}$$

This identifies the jet momentum-excess coefficient,

$$\Delta c_J \equiv \frac{\Delta J'}{\frac{1}{2}\rho_\infty V_\infty^2 c} = \frac{J' - \rho V_\infty^2 h}{\frac{1}{2}\rho_\infty V_\infty^2 c} = c_J - 2\frac{h}{c} \tag{6}$$

as the key parameter which quantifies the effect of the jet on the overall blown-lift flowfield.

2. Flow solution

The streamline angle can be determined from the vortex strengths as:

$$\theta(x) \equiv \alpha + \frac{w(x)}{V_\infty} = \alpha + \frac{1}{2\pi}\int_0^c \frac{\gamma(x')}{V_\infty}\frac{dx'}{x'-x} + \frac{\Delta c_J}{2}\frac{1}{2\pi}\int_c^\infty c\frac{d\theta}{dx'}\frac{dx'}{x'-x} \tag{7}$$

The challenge of solving equation 7 is that since θ is defined over the airfoil (taking the flap angle δ_f into account), it must be solved for $\gamma(x)$ for $0 < x < c$ and for $\theta(x)$ for $x > c$. When discretized, Equations 5 and 7 can be solved together with the Kutta condition and a specified initial jet angle at the trailing edge.

To calculate the pressure difference across the wing, we must remove the pressure turning the jet over the wing from the circulation pressure. As such,

$$\Delta c_p(\xi) \equiv \frac{\Delta p(\xi)}{\frac{1}{2}\rho V_\infty^2} = 2\frac{\gamma(\xi)}{V_\infty} - \Delta c_J\frac{d\theta}{d\xi} \tag{8}$$

where $\xi = x/c$. The inviscid sectional lift and moment coefficients are then obtained as follows.

$$c_\ell \equiv \frac{L'}{\frac{1}{2}\rho V_\infty^2 c} = \int_0^1 \Delta c_p(\xi)\,d\xi = \int_0^1 2\frac{\gamma(\xi)}{V_\infty}\,d\xi + \Delta c_J(\alpha - \theta_{TE}) \tag{9}$$

$$c_m \equiv \frac{M'}{\frac{1}{2}\rho V_\infty^2 c^2} = \int_0^1 \Delta c_p(\xi)\left(\frac{1}{4} - \xi\right)dx = \int_0^1 \frac{\gamma(\xi)}{V_\infty}\left(\frac{1}{4} - \xi\right)d\xi - \int_1^\infty \Delta c_J\left(\frac{1}{4} - \xi\right)\frac{d\theta}{d\xi}\,d\xi \tag{10}$$

IV. Methodology

A. Test Parameters

According to the blown-airfoil theory derivation in section III, the blown airfoil c_ℓ and c_m are functions of α, Δc_J, δ_f, and h/c. Although the propulsor position z_p and angle δ_m are not treated by this theory, they must have some effect in the real flow. The Reynolds number will also clearly have an influence. Based on this, the wind tunnel model was designed to control for these 5 variables, via the physical test parameters listed in table 1. Sections IV.B & IV.C describe the test design in detail.

Table 1 Controlled Test Parameters

Parameter	Tested Values
Engine Mount Angle [deg]	10, 20
Propeller Height [in]	2.11, 2.33
Flap Angle [deg]	0, 20, 40, 55, 90
Angle of Attack [deg]	-10, -5, 0, 5, 10, 15, 20, 25
Nominal Motor Current [A]	1, 4, 7, 10, 13, 16, 19
Nominal Tunnel Speed [m/s]	8.94
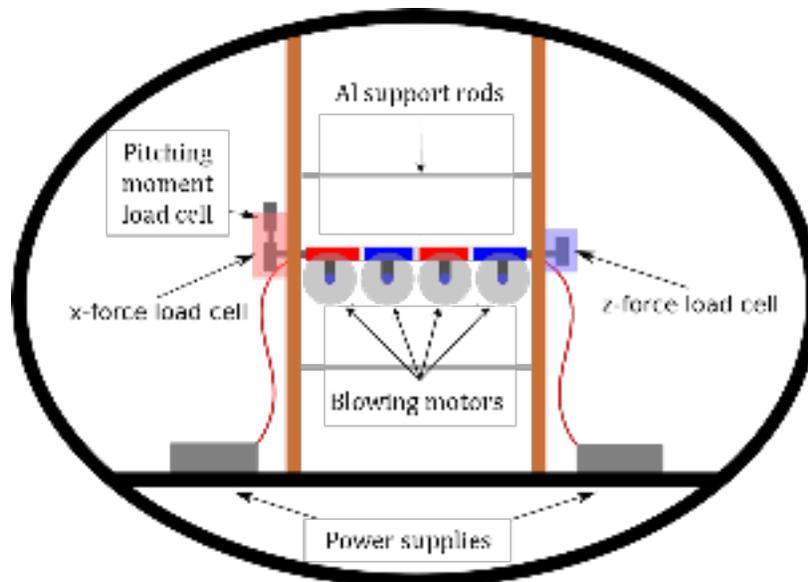
Fig. 3   Cross-section schematic of experimental set up.

Fig. 4   Photos of test rig. The left shows a front view of the setup, and the right shows a closeup of the wake survey rake.

B. Test Rig

The quasi 2-dimensional model was tested in the Wright Brothers Wind Tunnel (WBWT), which has a 7 ft × 10 ft elliptical cross section. Two plywood endplates were mounted vertically covering the full height of the cross section to constrain the flow between to be approximately 2-dimensional. The plywood boards were separated 1 ft above and below the wing section by thin 1/4 in aluminum rod spacers to tightly constrain their spacing for the wing. The setup is shown schematically in Figure 3. A front view is shown on the left in Figure 3.

A channeled 0.75 in diameter steel rod with universal joints on each was used as the main spar for the wing. At each end, the rod was supported by pillow blocks with collar bearings holding the rod. The pillow block on one side was mounted on a 10 lb load cell to measure drag and, on the other side, a lift load cell (10 lb) was used. The rod was restrained against pitch rotation by a 3.5 in lever arm, attached to a 2 lb load cell which thus measured the pitching moment. The lever arm angular position on the wing spar rod was varied to set the wing section angle of attack. Each data point was recorded by measuring a 5-second average of the voltage reading on all three load cells, at a frequency of 1000 Hz. Standard calibration techniques were used to decouple the readings of the 3 load cells, as explained in the appendix.

A pitot rake with 30 tubes at 0.08 in spacing was mounted on a 2D traverse, and was used to measure the velocity ratio $\frac{V}{V_\infty}$ in the wake of the model. The rake tips were positioned 0.3 in behind the trailing edge of the wing. During a test, the traverse ran a total of 5 passes across the span of the test section, with each pass shifted vertically so that the full extent of the wake could be captured. The rake was angled 30° back from vertical so that the tubes would be better aligned with the flow exiting the trailing edge of the deflected flap. The right side of Figure 4 shows the setup of the rake in the tunnel. The pitot tubes measure the total pressure loss or gain at their position. The total pressure is then converted to a "far downstream" velocity ratio by comparing it to a reference total pressure which is taken from the freestream.

C. Wing Section
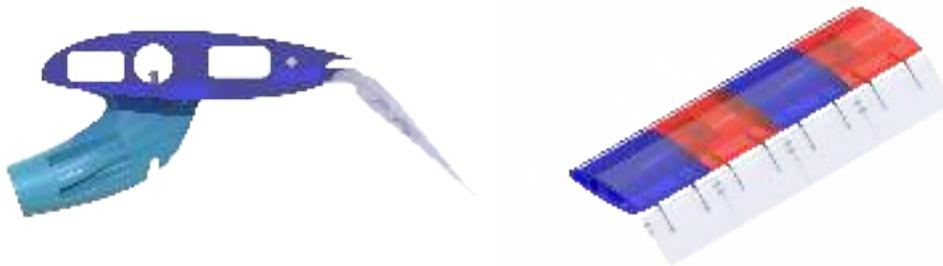
Fig. 5   CAD rendering of the wing sections displayed in side and rear isometric views.

The test wing has a 23.88 in span and a 9 in chord with the flap retracted. It was built in four identical sections, each composed of: the main element, flap, flap brackets, motor mount, and motor.

Each main element and flap section is a 5.97 in spanwise extrusion of a 2D airfoil (fig. 5). The airfoil components were printed in PLA (MatterHackers, PRO series PLA) using the Prusa i3 Mk II. The four section slide onto the spar to form the entire wing. Two channels for wiring were built into the wing sections to allow wires to travel within the segments. The aft channel was used for the majority of the wire travel. Then, a bridging area was used to break off from the aft channel (without spar interference) and get into the front channel that housed the actual motor mount connections.

The spar runs the length of the wingspan and a little beyond the endplate walls. Just outside the walls, the spar connects with U-joints that connect the spar to the load cells. Each main section is fixed to the spar using counter-sunk screws and aligned with the other sections by the spar and a dowel pin. A channel is milled into both ends of the spar to allow wires to pass through the wall channel and into the wing without interfering with the wall itself.

The flaps were made similarly to the main wing section, printed in PLA (MatterHackers, PRO series PLA) using the

Prusa i3 Mk II. Each flap has two dowel pins to connect between each of the four sections. The flaps and main sections were connected using eight flap brackets, water-jetted from 0.04 in steel sheet, and retained by a set screw in both the main section and the flap. A separate set of brackets was used to set each tested flap angle δ_f.
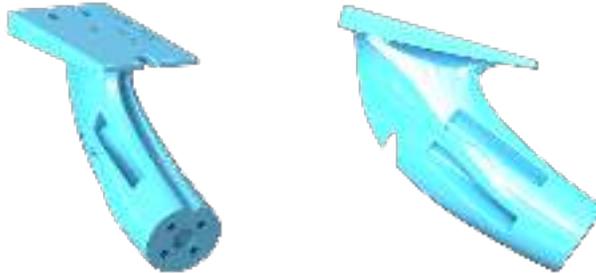
Fig. 6   Two CAD renderings demonstrating the motor mount design.

The motor mounts (Fig. 6) fit into a receiving inset printed in the main wing section, aligned via 2 dowel pins and secured to the main spar with a 6-32 stainless steel screw. The motor mount offers 4 channels for the screws to bind the motor to the motor mount. The channels were wrapped with tape after the motor was connected. Each motor mount is set to a specific angle and height, requiring a new mount for varying either of those variables. However, the mounts were interchangeable as the motor mount only involves one screw to attach to the wing. The motor mounts were printed with ABS to prevent melting from the hot motors.

The motors (T-Motor F40 Pro II, 1600 KV) are run at 24 V with APC 5×4E-4 propellers. The ESC (YEP Brand ESC, 40 A) control the angular velocity of the propellers, determined using an analog stroboscope.

D. Data Processing

1. Determination of force coefficients

At each test point, the blowing power was controlled via a common PWM signal sent to the motors. The resulting RPM was measured using a strobe, and correlated with Δc_J as described below. The load cell calibration matrix was generated by applying known forces at the model center quarter chord, and the 3/4 chord for the moment. Wind-off tares were taken before each data run. The tared voltage readings from each test run are used to compute the lift force, streamwise force and pitching moment via the calibration matrix. Details can be found in appendix .B. The non-dimensional coefficients c_ℓ, c_x, and c_m are then obtained from their definitions and assuming that that the sectional lift force $L' \approx \frac{L}{b}$.

2. Determination of jet momentum-excess coefficient

The jet momentum-excess can be determined by measuring the total pressure behind the propeller disc using a pitot tube. To ensure consistent relative placement of the pitot between tests, this was performed with one motor unit mounted on a load cell in a 1.5 ft x 1.5 ft open-jet wind tunnel, independent of the wing. The motor angular speed, free stream velocity and motor axis angle were varied, while the pressure behind the propeller disc, and thrust force were measured.

To determine the jet momentum-excess, the motors and propellers were characterized independent of the wing section. The jet momentum-excess coefficient is related to the jet mass coefficient, c_Q, by

$$\Delta c_J = 2c_Q \left(\frac{V_J}{V_\infty} - \frac{V_\infty}{V_J} \right) \tag{11}$$

7

where by classic propeller acutator disk theory,

$$\left(\frac{V_J}{V_\infty}\right)^2 = 1 + \frac{T}{\frac{1}{2}\rho V_\infty^2 \pi R^2} \tag{12}$$

and the jet mass coefficient is given by

$$c_Q = \frac{1}{2}\left(1 + \frac{V_J}{V_\infty}\right)\frac{h_d}{c} \tag{13}$$

where h_d is the effective propeller disc height, which by mass conservation can be estimated as

$$\frac{h_d}{c} = \frac{\pi(R^2 - r_h^2)\,n_p}{bc} \tag{14}$$

where r_h is the propeller hub radius and n_p is the number of propellers. The tested wing had $\frac{h_d}{c} = 0.35$.

Figure 7 shows the thrust coefficient against the advance ratio $V_\infty/\Omega R$ for a range of V_∞ between 0 and 15 m/s, where the spread in the data points is likely due to Reynolds number effects. In the main wind tunnel tests, the motor current draw and angular velocity were measured and the jet momentum-excess coefficient was determined using fig. 7.
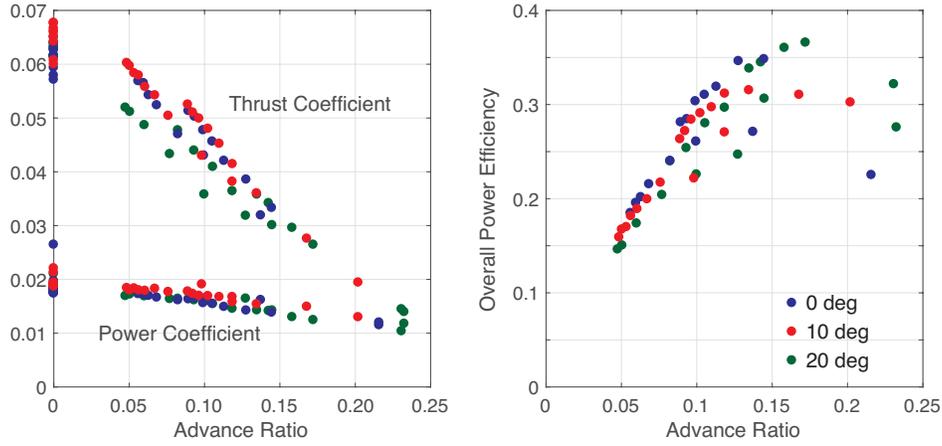
Fig. 7   Combined motor and propeller characterization test results. (a) Thrust and electrical power coefficients, (b) Overall power efficiency curve of motor. Colors show the different angle of attacks of the motor relative to free stream.

3. Data best-fit functions

For a given flap deflection angle, δ_f, and motor axis angle, δ_m, best fit surfaces were constructed to fit the experimental data. In particular, it is known that (c_ℓ, c_x, c_m) at fixed δ_f and δ_m are functions of the angle of attack α and jet momentum-excess coefficient Δc_J.

Traditionally, drag is expected to have a quadratic dependence on α, and so it is assumed that the relation is similar for for c_x. At small angles, c_ℓ and c_m are linear in α. However, it was found that a linear fit failed to capture the the stall behaviour, which happens at even small angles due to the large flap deflections. From an anti-symmetry argument, an α^2 term can be reasonably excluded from the c_ℓ and c_m curve fits. The α^3 term, however, captures the effect of stall, and so the c_ℓ and c_m curve fits were chosen to be cubic in α, with good physical basis.

Since the effect of Δc_J on c_ℓ, c_x, and c_m is unknown, it was assumed that the aforementioned angle-of-attack polynomial coefficients are each themselves polynomial functions of Δc_J. The degree of these polynomials was chosen by trial-and-error to achieve a good fit to the data without over-fitting. For example, consider the curve fit for c_ℓ. The

following function is to be minimized:

$$\min \sum_{i=1}^{N} \left(c_{\ell_i} - f_1(\Delta c_{J_i}) - f_2(\Delta c_{J_i}) \, \alpha - f_3(\Delta c_{J_i}) \, \alpha^3 \right)^2 \tag{15}$$

$$\text{where} \quad f_k(\Delta c_{J_i}) = \sum_{j=0}^{M} a_{kj} \Delta c_{J_i}{}^{j} \qquad (k = 1, 2, 3) \tag{16}$$

The a_{kj} values are found by minimizing equation 15 with respect to the a_{kj}. The value of M is chosen manually to arrive at the most suitable fit. It was found that $M = 1$, indicating a linear effect of Δc_J, resulted in the best fits. This is in essence similar to a multivariate least squares regression scheme.

It is important to quantify the closeness of the best-fit functions in the approximation of the data in the range of collected data. This is done using the Normalized Root Mean Squared Error (NRMSE). Let θ be the measured quantity (for example, c_ℓ and $\hat{\theta}$ be the approximation to the quantity using the fit function, then NRMSE is defined as:

$$\text{NRMSE} = \frac{1}{\theta_{max} - \theta_{min}} \sqrt{\frac{\sum_{i=1}^{N} \left(\hat{\theta}_i - \theta_i \right)^2}{N}} \tag{17}$$

Table 2   NRMSE of the fits c_ℓ generated for different δ_f and δ_m

	δ_f				
	0°	20°	40°	55°	90°
$\delta_m = 10°$	0.034	0.061	0.034	0.044	0.029
$\delta_m = 20°$	0.040	(-)	0.040	(-)	(-)

Table 3   NRMSE of the c_x fits generated for different δ_f and δ_m

	δ_f				
	0°	20°	40°	55°	90°
$\delta_m = 10°$	0.040	0.072	0.043	0.060	0.069
$\delta_m = 20°$	0.039	(-)	0.071	(-)	(-)

Table 4   NRMSE of the c_m fits generated for different δ_f and δ_m

	δ_f				
	0°	20°	40°	55°	90°
$\delta_m = 10°$	0.040	0.083	0.062	0.066	0.060
$\delta_m = 20°$	0.16	(-)	0.12	(-)	(-)

Tables 2,3, and 4 show generally low NRMSE values for the fit functions, which indicates that the fits serve as a good approximation to the discrete data points. It is worth noting, however, that table 4 exhibits high NRMSE values for the c_m fits in the $\delta_m = 20°$ cases, suggesting that the fits fail to accurately represent the data in these cases.

V. Results

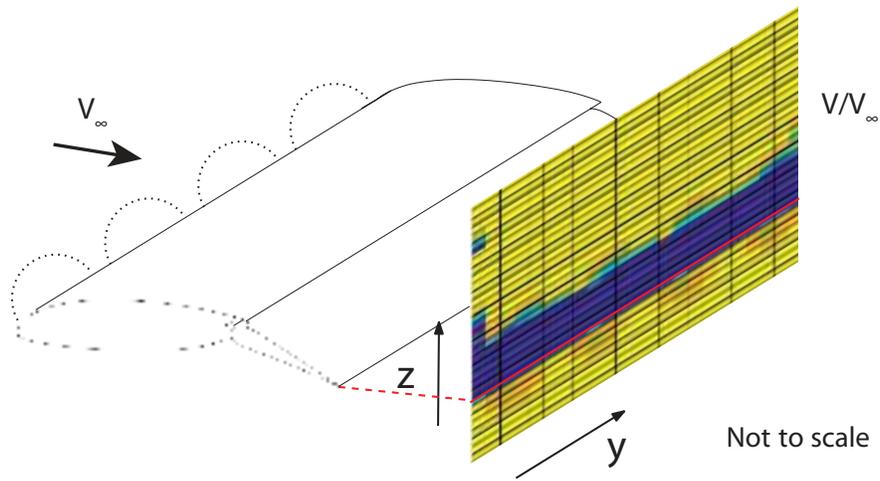## A. Force and Moment Coefficients

Figures/editted_c-alpha-eps-converted-to.pdf
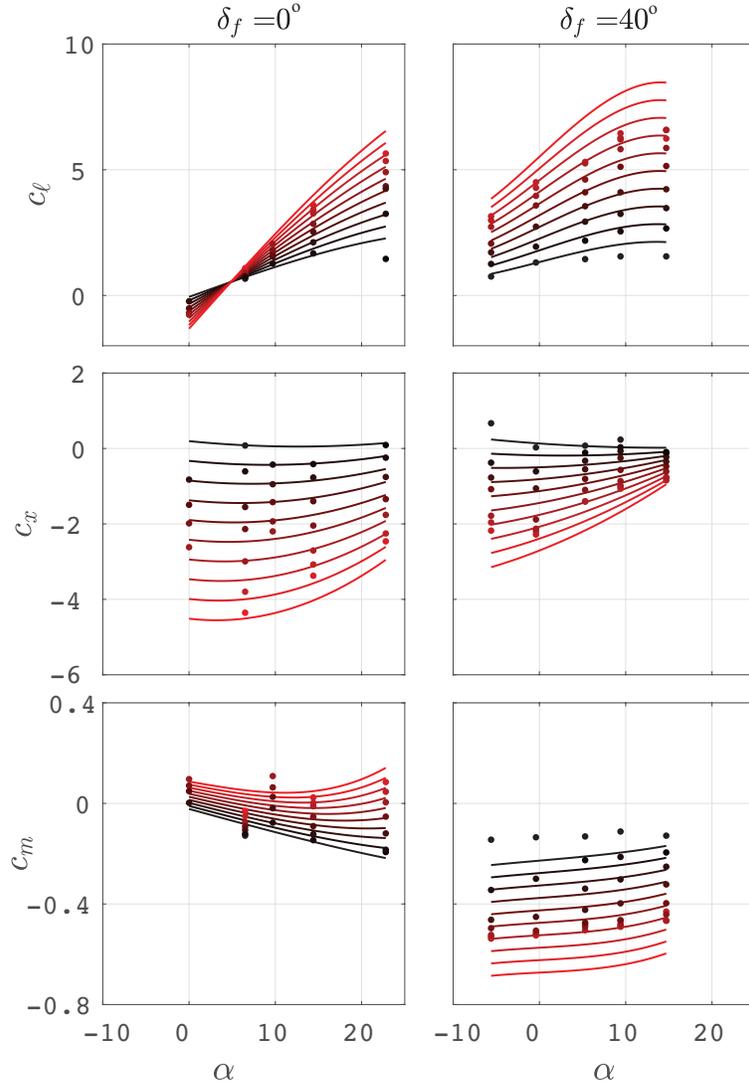
Fig. 9 c_ℓ, c_x, c_m **against angle of attack for 20° motor axis angle. Points represent collected data and the lines represent the best-fit functions (explained in section IV.D.3) at constant Δc_J, plotted at Δc_J increments of 0.5.**
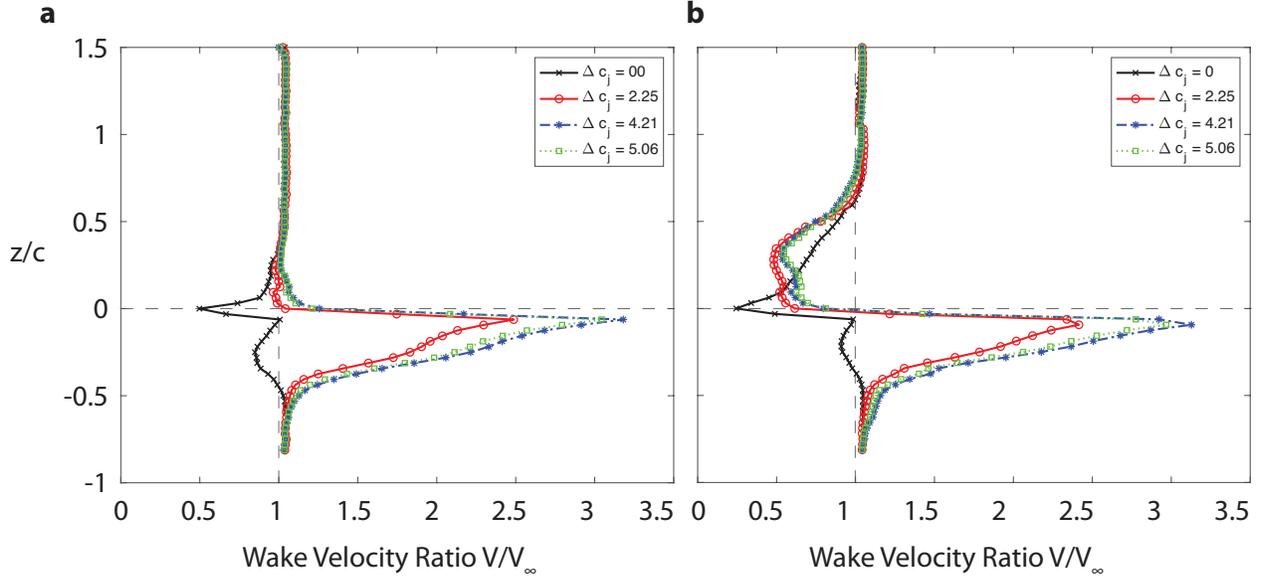
B. Wake Characterization

Fig. 10   Illustration depicting the alignment of 2D rake data plots to the physical model
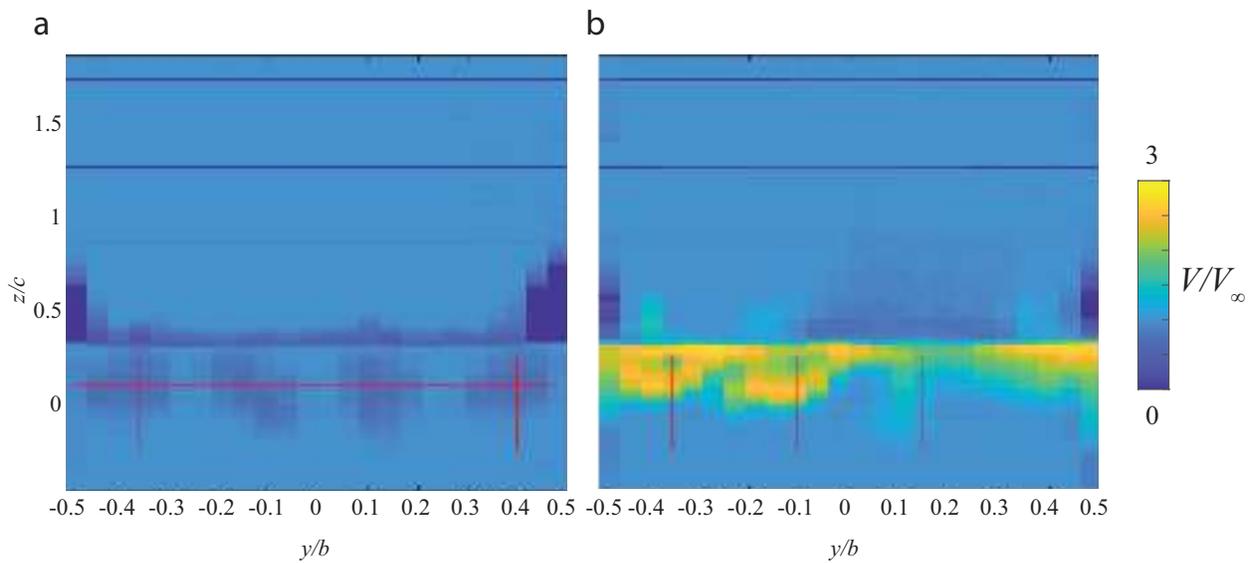
Fig. 11   Wake profiles for (a) unpowered, and (b) powered wing at $\Delta c_J = 4$. Both profiles are at $\delta_f = 20°$ and $\alpha = 0$. The spanwise consistency demonstrates uniform jet profile. Projected motor locations are indicated with red lines.

12

Fig. 12 Vertical wake profile for (a) $\alpha = 0°$ **and (b)** $\alpha = 10°$**. Both are at** $\delta_f = 20°$

VI. Discussion

A. Force Coefficient Polars

The performance of the blown wing is summarized by the $c_\ell - c_x$ polars shown in figures 13 and 14.

Figure 13 best demonstrates the effect of blowing on the wing. For $\delta_f \leq 55°$, increased ΔC_J expands the curve to the more negative c_x (more thrust) and to higher c_ℓ. The contribution of blowing to both c_ℓ and c_x are well approximated by a linear functions, as in last term of equation 9. For $\delta > 55°$, it appears that this effect is dampened which is likely due to the separation of the flap. This is especially evident in the $\delta_f = 90°$ case where the curve compresses and inverts.

An important finding is that after induced drag is added to the measured c_x values for any reasonable aspect ratio, the aircraft will have a positive overall streamwise force (positive net drag). Thus landing is possible at very high c_ℓ values. For example, for the $\delta_f = 40°$ case at $\Delta c_J = 4.0$ we have $c_\ell \approx 8$, $c_x \approx 0$. For $R = 10$, these will give $C_L \approx 7$ and $C_X \approx 1.3$, with a $\frac{C_X}{C_L} = 0.18$ which is an $11°$ descent angle. For takeoff at $\delta_f = 20°$ and $\Delta C_J = 4.0$, we have $c_\ell = 6$, $c_x = -2$, giving $C_L \approx 5$ and $C_X \approx -1.5$ and $\frac{C_X}{C_L} = -0.3$, which is an $18°$ climb angle. These estimates suggest exceptional STOL performance.

B. Effect of Motor Axis Angle

The effect of the motor axis angle δ_m is compared for mounts of $10°$ and $20°$ in Figure 15. The most obvious distinction is in the $40°$ flap setting where the $20°$ mount setup appears to stall more suddenly and more aggressively than the $10°$ setup. This suggests that upper surface separation may be occurring earlier due to the jet having to bend the extra angle to stay attached to the upper surface. For lower δ_f tests, a different relationship is seen where the $c_\ell - c_x$ slope is slightly steeper, suggesting higher lift values for similar amounts of blowing. Also evident is the slight increase in overall thrust in $10°$ vs. $20°$ setups with very little loss of maximum attainable lift. This suggests that in the range tested, δ_f has a relatively small impact on attainable lift.
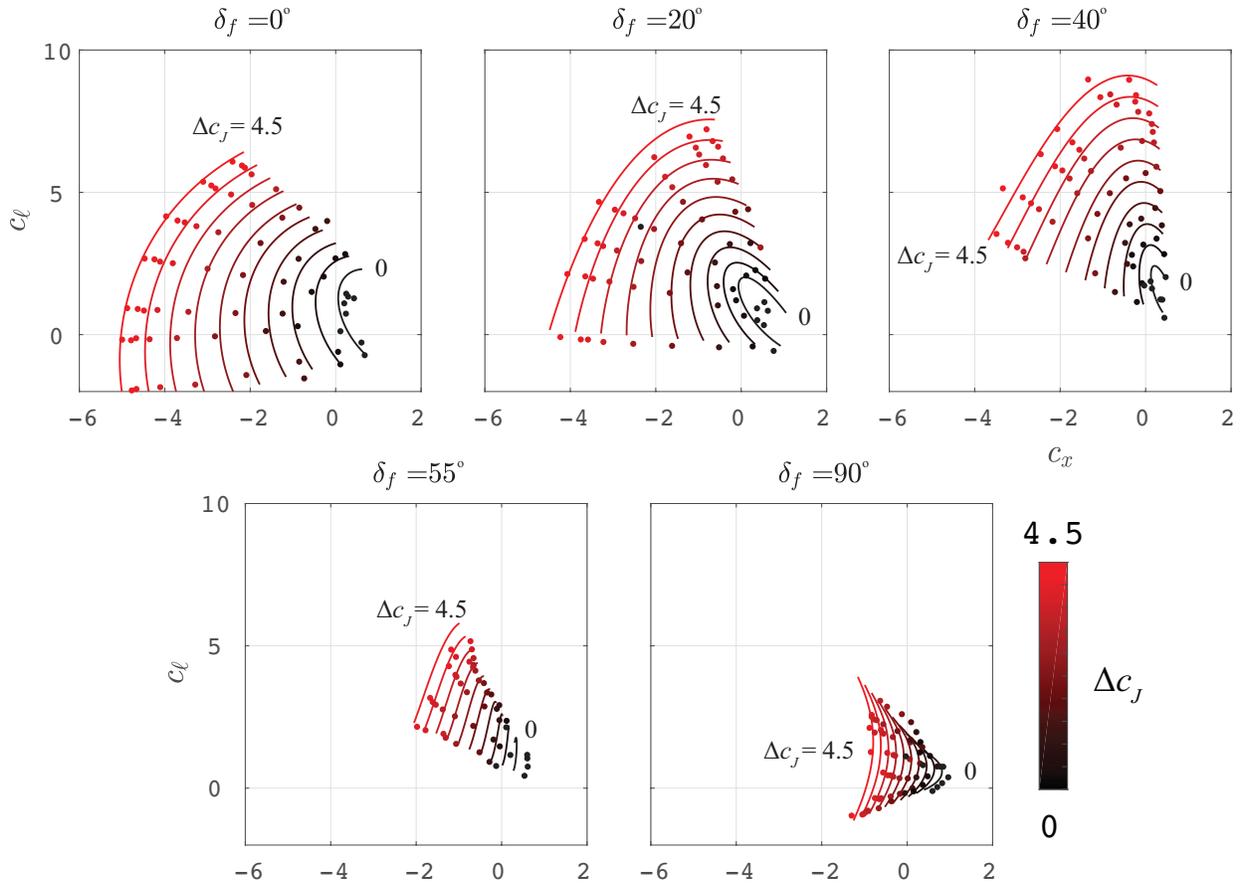
Fig. 13 c_l-c_x **polars for 10°motor axis angle. Points represent collected data, lines are polynomial fit.**
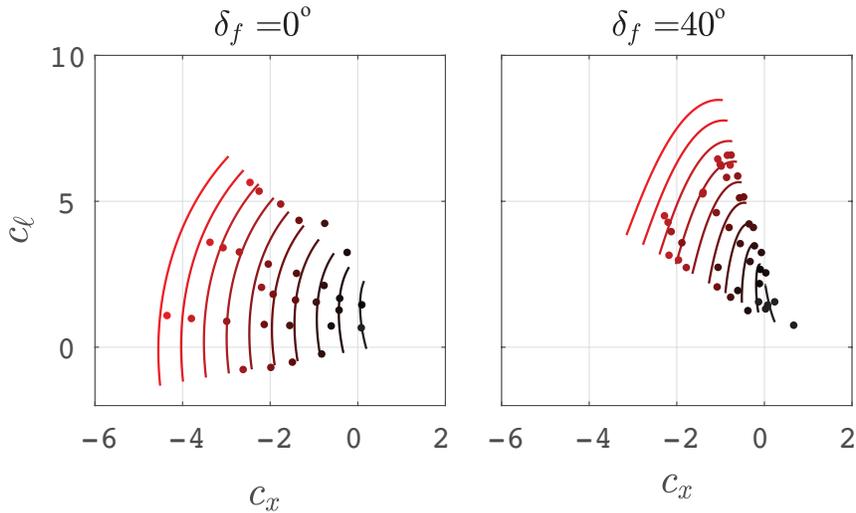
Fig. 14 c_l-c_x **polars for 20°motor axis angle. Points represent collected data, lines are polynomial fit.**

C. Blown Wing Performance Relative to Hover

One major benefit of blown wings is the reduction in power needed for lift, as compared to direct vertical hover. This ratio can be measured by the ratio of jet excess powers (defined in the appendix) in two cases: (1) a blown wing of chord

14
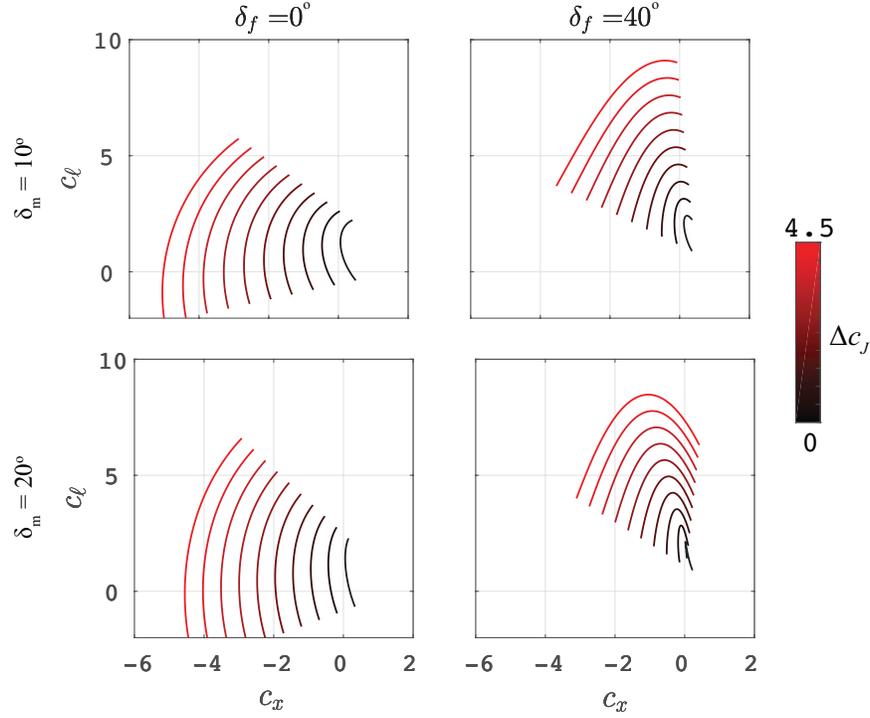
Fig. 15 $c_\ell - c_x$ **fit function polars for** $\delta_m = 10°$ **and** $\delta_m = 20°$**, for** α **ranging from -5°to 23°. The data points have been excluded for ease of visualization.**

c and effective jet disk height h_d requiring a lift force L and (2) a hovering 2D propeller of the same width h_d, hovering (i.e., $V_\infty = 0$) with a thrust of $T = L$. As such, the ratio of powers is

$$\frac{\Delta c_{EB}}{\Delta c_{EH}} = \frac{\left(1 + \frac{V_{JB}}{V_\infty}\right)\left(\frac{V_{JB}^2}{V_\infty^2} - 1\right)}{V_{JH}^3 / V_\infty^3} \tag{18}$$

and the jet speeds are related by the requirement that blown lift is the same as hovering thrust,

$$T = \dot{m}(V_J - V_\infty) = L = \frac{1}{2}\rho V_\infty^2 c\, c_\ell(\Delta c_J, \alpha, \delta_f) \tag{19}$$

$$\therefore \frac{V_{JH}^2}{V_\infty^2} = \frac{1}{h_d/c}\, c_\ell(\Delta c_J, \alpha, \delta_f) \tag{20}$$

The ratio of powers is plotted in Figure 16, and demonstrates how for the power required to lift by blowing is significantly less than the power required for hovering. As expected, the 90°flap case shows little improvement, while the 40°flap exhibits best performance of the tested flap angles.

D. Separation of Upper Surface

The spanwise average of the wake velocity defect shown in section V.B gives insight into the physical characteristics of the boundary layer on the blown wing. It is clear when comparing (a) and (b) that a separation region begins to form on the upper surface at a relatively long α value. This is evidenced by the velocity ratio having a value less than 1 on the upper surface. Interestingly, the separation increases in the presence of blowing . The presence of the separation on the upper surface of the wing suggests that the vertical positioning of the propulsor, z_m, could be shifted up. This would hopefully lead to an increase in c_ℓ by decreasing viscous decambering but might come at the expense of increased thrust for that c_ℓ which would be problematic for landing. This suggests that there may be optimum values for different operating points. Further work in this area will be needed to understand the full extent of the effects.
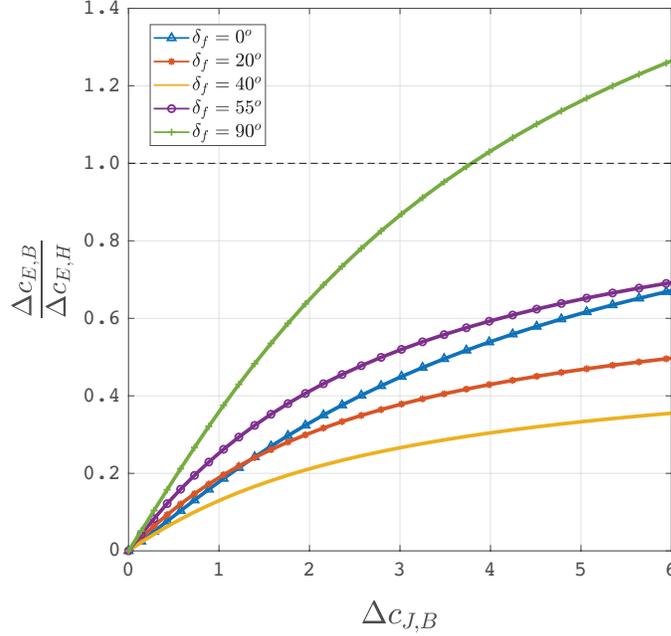
Fig. 16   Ratio of excess power in blown-lift to excess power of hovering for equivalent thrust and disk area, at different flap angles and at α which maximizes c_ℓ

E. Pitching Moment Behavior

At $\delta_f = 0°$, increasing the blowing increases the aircraft's c_m. This is expected since the blowing motor produces a significant forward force below the quarter chord. For non-zero δ_f values, and low angles of attack, the impact of blowing on c_m is reversed. This is because the downwards deflection of the blowing jet by the flap represents an upwards force acting on the airfoil aft of its quarter chord, contributing a negative pitching moment. However, at higher angles of attack, flow separation is expected to occur on the flaps, meaning that the negative pitching moment contribution of the flaps decreases. This is why we observe the lines of fixed Δc_J in the $c_m - \alpha$ plots of fig. 8 to converge at higher angles of attack.

VII. Conclusion

Tunnel tests of blown flapped wing were conducted in MIT's Wright Brothers Wind Tunnel. The tests sought to characterize the effect the blown-wing parameters α, δ_f, δ_m, and Δc_J on aerodynamic performance. The tunnel model was designed to adjust these parameters and record the effects.

It was found that the blown wing had exceptional high-lift performance: at some flap angles, $c_{\ell_{max}}$ increased by nearly a factor of 4 over the unblown case (fig. 13). This performance is also achieved with significantly lower power input than would be required to create a comparable lifting force with direct thrust from the same propulsors. High c_ℓ values are also achievable with small negative or slightly positive c_x values, which is important during landing when both high lift and high net drag are desirable.

Wake surveys conducted on the model indicate that that the concept has further room for improvement or optimization for specific purposes. Upper surface separation shown in the rake surveys suggest that better motor positioning would improve the concept. Additionally, the airfoil used was not optimized for blown performance, suggesting that further performance improvements can be achieved with modified airfoils.

16

Appendices

A. Derivation of jet excess power coefficient

The required power generating a jet is, in general,

$$\Delta P = \frac{1}{2}\dot{m}(V_J^2 - V_\infty^2) \tag{21}$$

Considering the section at the disc, $\dot{m} = \rho h_D V_D = \rho h_D \left(\frac{V_\infty + V_J}{2}\right)$, and therefore

$$\Delta P = \frac{1}{4}\rho h_D (V_\infty + V_J)(V_J^2 - V_\infty^2) \tag{22}$$

Defining the jet excess power coefficient,

$$\Delta c_E \equiv \frac{\Delta P}{\frac{1}{2}\rho V_\infty^3 c} \tag{23}$$

we can determine the jet excess power for the blowing and hovering cases. In the hovering case (and not in the blowing case) $V_\infty = 0$. Therefore,

$$\Delta c_{EB} = \frac{\frac{1}{4}\rho h_D (V_\infty + V_{JB})(V_{JB}^2 - V_\infty^2)}{\frac{1}{2}\rho V_\infty^3 c} \tag{24}$$

$$= \frac{1}{2}\frac{h_d}{c}\left(1 + \frac{V_{JB}}{V_\infty}\right)\left(\frac{V_{JB}^2}{V_\infty^2} - 1\right) \tag{25}$$

$$\Delta c_{EH} = \frac{\frac{1}{4}\rho h_D V_{JH}^3}{\frac{1}{2}\rho V_\infty^3 c} \tag{26}$$

$$= \frac{1}{2}\frac{h_d}{c}\frac{V_{JH}^3}{V_\infty^3} \tag{27}$$

And thus the ratio of blowing excess power to hovering excess power is

$$\frac{\Delta c_{EB}}{\Delta c_{EH}} = \frac{\left(1 + \frac{V_{JB}}{V_\infty}\right)\left(\frac{V_{JB}^2}{V_\infty^2} - 1\right)}{V_{JH}^3/V_\infty^3} \tag{28}$$

B. Load cell calibration matrix

There is expected to be mechanical coupling between the load cells, and this must be accounted for by computing a voltage-load calibration matrix $\mathbf{B}$. Then, we have, with v_1, v_2 and v_3 representing the tared voltage measured by the z-force, x-force and pitching moment load cells:

$$\begin{Bmatrix} v_1 \\ v_2 \\ v_3 \end{Bmatrix} = \begin{bmatrix} B_{11} & B_{12} & B_{13} \\ B_{21} & B_{22} & B_{23} \\ B_{31} & B_{32} & B_{33} \end{bmatrix} \begin{Bmatrix} L \\ X \\ M \end{Bmatrix} \tag{29}$$

The entries of the matrix are calculated using known calibration loads, as follows:

$$\begin{Bmatrix} B_{11} \\ B_{21} \\ B_{31} \end{Bmatrix} = \begin{Bmatrix} v_1/F_L^{\text{cal}} \\ v_2/F_L^{\text{cal}} \\ v_3/F_L^{\text{cal}} \end{Bmatrix} \tag{30}$$

$$\left\{ \begin{array}{c} B_{12} \\ B_{22} \\ B_{32} \end{array} \right\} = \left\{ \begin{array}{c} v_1/F_X^{\text{cal}} \\ v_2/F_X^{\text{cal}} \\ v_3/F_X^{\text{cal}} \end{array} \right\} \tag{31}$$

$$\left\{ \begin{array}{c} B_{13} \\ B_{23} \\ B_{33} \end{array} \right\} = \left\{ \begin{array}{c} \left(v_1/F_M^{\text{cal}} - B_{1L}\right)/\ell \\ \left(v_2/F_M^{\text{cal}} - B_{2L}\right)/\ell \\ \left(v_3/F_M^{\text{cal}} - B_{3L}\right)/\ell \end{array} \right\} \tag{32}$$

Where ℓ represents the length of the moment arm between the known load and the moment load cell. The calibration matrix, along with tare runs, are generated whenever major configuration changes are made to the wing section (such as changing flaps).

C. Polynomial data fit functional forms

Based on section IV.D.3, the polynomial fits are given by

$$c_l(\alpha, \Delta c_J) = \begin{bmatrix} 1 & \Delta c_J & \alpha & \alpha \Delta c_J & \alpha^3 & \alpha^3 \Delta c_J \end{bmatrix} \mathbf{a}_{cl} \tag{33}$$

where $\mathbf{a}_{cl}$ is a 6×1 vector of coefficients. The dependency on flap angle is not explicitly included, but separate coefficient vectors are determined for each flap angle.

Similarly, the polynomial fit for c_x and c_m are

$$c_x(\alpha, \Delta c_J) = \begin{bmatrix} 1 & \Delta c_J & \alpha & \alpha \Delta c_J & \alpha^2 & \alpha^2 \Delta c_J \end{bmatrix} \mathbf{a}_{cx} \tag{34}$$

$$c_m(\alpha, \Delta c_J) = \begin{bmatrix} 1 & \Delta c_J & \alpha & \alpha \Delta c_J & \alpha^3 & \alpha^3 \Delta c_J \end{bmatrix} \mathbf{a}_{cm} \tag{35}$$

Note, in the c_ℓ and c_m fits α^3 is used, while in the c_x fits, α^2 is used due to the symmetry of the problem. All angles in fits are based in degrees.

Table 5 c_ℓ fit coefficients

	$\delta_m = 10°$					$\delta_m = 20°$	
	$\delta_f = 0°$	$\delta_f = 20°$	$\delta_f = 40°$	$\delta_f = 55°$	$\delta_f = 90°$	$\delta_f = 0°$	$\delta_f = 40°$
a_1	1.95E-01	4.70E-01	1.34E+00	1.17E+00	8.95E-01	-5.64E-02	1.33E+00
a_2	-1.86E-01	3.64E-01	8.40E-01	5.59E-01	3.31E-01	-2.81E-01	9.31E-01
a_3	1.15E-01	1.50E-01	9.23E-02	8.91E-02	4.98E-02	1.23E-01	8.88E-02
a_4	4.39E-02	3.91E-02	4.40E-02	2.32E-02	2.41E-02	5.81E-02	5.04E-02
a_5	-5.10E-05	-2.08E-04	-1.01E-04	-2.89E-04	-8.98E-06	-4.06E-05	-1.60E-04
a_6	-3.61E-06	7.89E-06	-2.84E-05	1.48E-05	7.62E-06	-7.88E-06	-8.25E-05
NRMSE	0.034	0.061	0.034	0.044	0.029	0.040	0.040

Table 6 c_x **fit coefficients**

	$\delta_m = 10°$					$\delta_m = 20°$	
	$\delta_f = 0°$	$\delta_f = 20°$	$\delta_f = 40°$	$\delta_f = 55°$	$\delta_f = 90°$	$\delta_f = 0°$	$\delta_f = 40°$
a_1	2.52E-01	2.98E-01	2.18E-01	3.42E-01	7.30E-01	1.95E-01	1.33E-01
a_2	-1.18E+00	-9.65E-01	-7.17E-01	-4.59E-01	-3.48E-01	-1.05E+00	-6.31E-01
a_3	-3.93E-02	-7.73E-02	-2.12E-02	4.77E-03	-2.62E-02	-2.28E-02	-1.58E-02
a_4	1.01E-02	3.57E-02	2.92E-02	9.10E-03	2.09E-03	-7.81E-04	2.36E-02
a_5	2.00E-03	4.13E-03	1.19E-03	-5.17E-04	-2.04E-03	9.00E-04	5.54E-04
a_6	4.16E-04	-4.92E-04	-9.20E-05	2.02E-04	5.70E-05	7.23E-04	3.18E-04
NRMSE	0.040	0.072	0.043	0.060	0.069	0.039	0.071

Table 7 c_m **fit coefficients**

	$\delta_m = 10°$					$\delta_m = 20°$	
	$\delta_f = 0°$	$\delta_f = 20°$	$\delta_f = 40°$	$\delta_f = 55°$	$\delta_f = 90°$	$\delta_f = 0°$	$\delta_f = 40°$
a_1	-2.24E-02	-6.14E-02	-2.09E-01	-1.60E-01	-1.30E-01	-2.22E-02	-2.28E-01
a_2	4.83E-02	-3.97E-02	-9.81E-02	-7.74E-02	-3.33E-02	2.42E-02	-9.89E-02
a_3	-3.42E-03	-5.20E-03	7.59E-04	2.19E-04	-8.37E-05	-9.37E-03	3.01E-03
a_4	4.12E-04	1.73E-03	-6.46E-04	5.56E-04	2.69E-03	7.48E-04	-2.73E-04
a_5	-5.06E-07	4.97E-06	-1.11E-06	1.05E-05	-7.00E-06	1.54E-06	4.59E-06
a_6	2.32E-06	2.77E-06	7.76E-06	3.12E-06	-4.43E-06	3.25E-06	2.50E-6
NRMSE	0.040	0.083	0.062	0.066	0.060	0.160	0.120

Acknowledgments

References

[1] Gnadt, A., Isaacs, S., Price, R., Dethy, M., and Chappelle, C., "Hybrid Turbo-Electric STOL Aircraft for Urban Air Mobility," *AIAA Scitech 2019 Forum*, American Institute of Aeronautics and Astronautics, Reston, Virginia, 2019. doi:10.2514/6.2019-0531, URL https://arc.aiaa.org/doi/10.2514/6.2019-0531.

[2] Courtin, C., Burton, M. J., Yu, A., Butler, P., Vascik, P. D., and Hansman, R. J., "Feasibility Study of Short Takeoff and Landing Urban Air Mobility Vehicles using Geometric Programming," *2018 Aviation Technology, Integration, and Operations Conference*, 2018, p. 4151.

[3] Courtin, C., and Hansman, R. J., "Safety Considerations in Emerging Electric Aircraft Architectures," AIAA Aviation Forum, American Institute of Aeronautics and Astronautics, 2018. URL http://arc.aiaa.org.

[4] Roe, M. H., and Renselaer, D. J., "STOL Tactical Aircraft Investigation, Externally Blown Flap. Volume II. Design Compendium," Tech. rep., Rockwell International Corporation, 1973.

[5] Thwaites, B., "Incompressible Aerodynamics," 1960.

[6] Maskell, E. C., and Spence, D. A., "A Theory of the Jet Flap in Three Dimensions," *Proceedings of the Royal Society A: Mathematical, Physical and Engineering Sciences*, Vol. 251, No. 1266, 1959, pp. 407–425. doi:10.1098/rspa.1959.0116, URL http://rspa.royalsocietypublishing.org/cgi/doi/10.1098/rspa.1959.0116.